Supplement of Atmos. Meas. Tech., 17, 5261–5277, 2024
https://doi.org/10.5194/amt-17-5261-2024-supplement

Atmospheric Measurement Techniques
Open Access
EGU

Supplement of

Current potential of CH_4 emission estimates using TROPOMI in the Middle East

Mengyao Liu et al.

Correspondence to: Mengyao Liu (mengyao.liu@knmi.nl)

S1. Select reliable TROPOMI XCH_4 observations

The selection based on two aspects, daily AOD value for each pixel and a new water-land mask to identify pixels over coastlines.

The way to find AOD for each pixel is consisted of two steps. (1) Check if any MODIS observations of AOD at 550nm are available within a 0.2° radial area of the pixel center. Use the median value of these MODIS AODs to stand for the AOD of this pixel if the presumption is true. (2) If there are no available MODIS observations, use the AOD value from global hourly Atmospheric Composition Reanalysis 4 (EAC4) that is constrained by MODIS observation instead. The method to build the constrained daily AOD from EAC4 is as follow:

First, we build monthly mean of MODIS AOD on a grid of 0.75°, which is the same resolution as EAC4 dataset. For the grid cell without any observations in a month, we apply a spatial interpolation staring from surrounding ± 2 grid cells until finding the available MODIS observations. In the meanwhile, the monthly mean of EAC4 AOD is generated by sampling grid cells at the same overpass time as MODIS pixels and preforming the same spatial interpolation process. Thus, the consistence between monthly MODIS AOD and CAMS AOD is ensured. Then the daily AOD of a TROPOMI pixel that has no MODIS observation is estimated by:

$$AOD_T = \frac{AOD^m_{MODIS}}{AOD^m_{ECA}} \cdot AOD^d_{ECA} \qquad \text{(S1)}$$

AOD_T stands for the estimated daily AOD for a TROPOMI pixel missing a MODIS observation. AOD^m_{MODIS} and AOD^m_{ECA} are monthly means of MODIS and ECA AOD after the same spatial interpolation aforementioned, respectively. AOD^d_{ECA} is the daily AOD from ECA. The calculation of Eq. (S1) is on a grid of 0.75°.

We selected pixels locating at several 1° ×1° areas covering half land and half ocean at the coastlines of such as Oman, Yemen and along Red Sea. We found there are not too many anomalous between pixels over land and ocean. Figure S2 shows an example of a 1° ×1°

area of [18.5-19.5°N 56.8-57.8°E] covering one part of the coastline of Oman. There are only three months in 2019 that have the valid observation. The values of AOD over land and ocean are quite consistent due to the transport. Although we can see the significance of albedo between pixels over land and over ocean, there are not big difference for XCH4

S2. Procedure to build the non-divergent wind field

The Flux-Divergence method operates on the assumption that any divergence in the flux of a target gas results from the presence of its sources and sinks. However, the flux (F) is determined by the product of the gas (ΔXCH_4^{PBL} in this study, use V to represent the vertical column density in Eq. (1)) and the wind velocity (w).

By applying the chain rule, we obtain:

$$\nabla \cdot F = \nabla \cdot (V\vec{w}) = (\nabla V) \cdot \vec{w} + V(\nabla \cdot \vec{w}) \quad \text{(S2)}$$

A segment of the flux divergence is attributed to variations in the wind field, unrelated to the emission or deposition. At a global level, wind divergence arises from the movement between low-pressure and high-pressure zones. Additionally, larger-scale factors like mountain ranges, coastlines, and other topographic features can contribute to divergence. On a more localized level, interpolating the ECMWF wind field grid onto a regular grid may also introduce some divergence in the wind field. In order to find a flux-field for which $\nabla \cdot \vec{w}$ is minimized, and thus $\nabla(\nabla \cdot \vec{w})$ approaches zero, we followed the method proposed by Sims (2018):

Assume $\vec{w}$ contains divergence. Iterate:

1. Compute the divergence of $\overrightarrow{w_k}$: $\nabla \cdot \overrightarrow{w_k}$

2. Compute the gradient of the divergence: $\nabla(\nabla \cdot \overrightarrow{w_k})$.

3. Update vector field: $\overrightarrow{w_{k+1}} = \overrightarrow{w_k} + m\nabla(\nabla \cdot \overrightarrow{w_k})$.

m is used to scale the update. Stopping Criterion: $|\overrightarrow{w_{k+1}} - \overrightarrow{w_k}| < 10^{-5}$ or $k > 10000$.

The principle of this algorithm is based on the observation that an area has negative divergence when more flux enters a domain than leaves it. Conversely, a domain has positive divergence when it has a net outflow of particles. Therefore, divergence can be diminished by adding flow away from the area with a negative divergence, and towards areas with a positive divergence. Repeatedly adding the gradient of the divergence to a

vector field achieves this, as the gradient is an arrow pointing from low-divergence areas to high-divergence areas.

This algorithm is similar to the Newton-Rhapson technique that iteratively approximates the root of a function by continuously adding the derivative of a function to an initial guess for the root. As the gradient of the divergence becomes smaller when a local minimum is reached, the update to the vector field also becomes smaller.

A side note on the implementation of the algorithm is that the units of the original vector field (F) and the vector field we use as update ($\nabla\,(\nabla \cdot F)$) are different. In the specific implementation of wind vector field ($\vec{w}$), the units of the original vector field are m/s, whereas the gradient of the divergence has units 1/(m·s). To compensate for this, it was chosen to multiply the gradient of the divergence by the dimensions of the grid cells Δx and Δy. Thus, the scaling factor then becomes $m \cdot \Delta x \cdot \Delta y$.

It is also important to note that the algorithm is applied to the wind field after interpolation, as interpolation also introduces small-scale divergence. In each iteration, the absolute value of the divergence is summed over the research domain. When the decline of this metric is smaller than 10^{-5}, the algorithm is terminated. The sum over the divergence lies in the order of magnitude of 10^{-1}. A limit of 10000 iterations is also implemented, in case the metric does not converge.

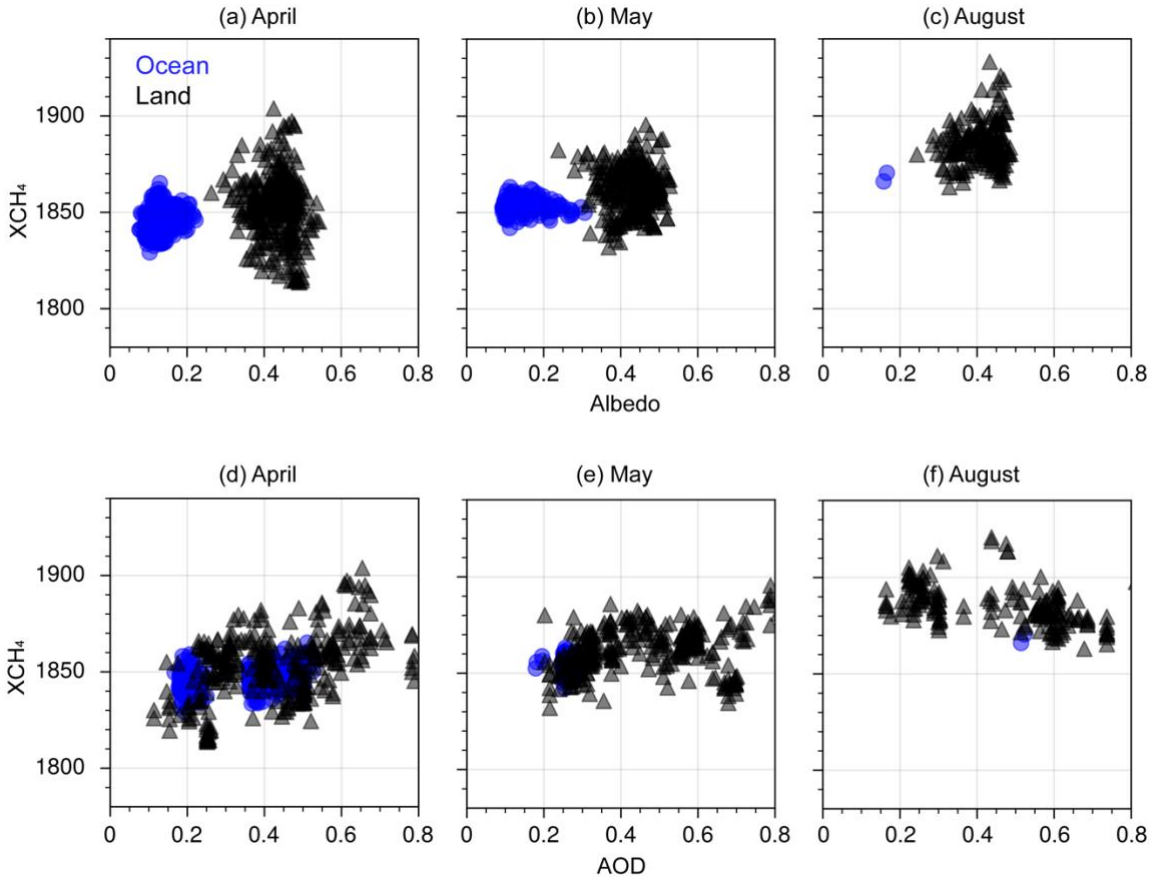

Figure S1. The monthly scatter plots for XCH_4 and albedo in (a) April, (b) May and (c) August in 2022. (d)-(f) are similar to (a)-(c) but for XCH_4 and AOD. Each blue dot or black triangle stands for one pixel locating in the area of [18.5-19.5°N 56.8-57.8°E].

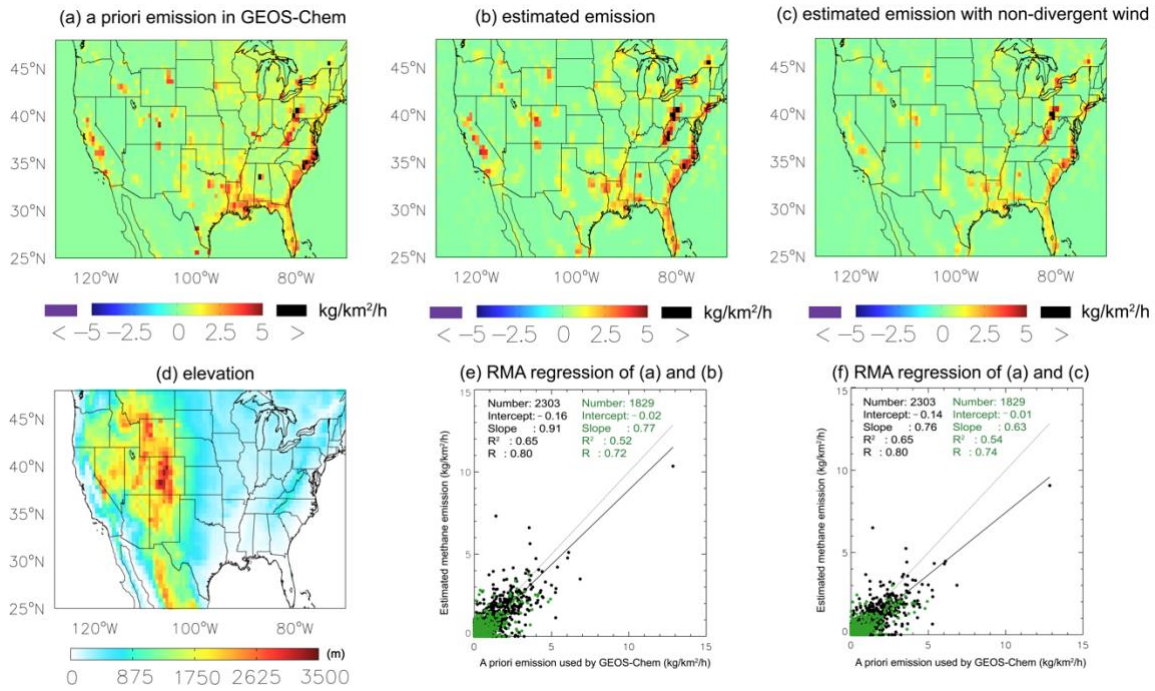

Figure S2. The spatial distributions of (a) the average of a priori CH_4 emissions used in GEOS-Chem simulation, (b) corresponding estimated CH_4 emissions over June-August 2012 on a 0.625° lon. 0.5° lat. grid in Liu et al., (2021). (c) The estimated CH_4 emissions by using the non-divergent wind. (d) The elevation map that is generated from GMTED2010 data set. (e) Scatter plots for emissions between a priori emissions estimated CH4 emissions in (b) The black and green dots stand for the grid cells in the east [100°W-70°W, 25°N-48°N] and west [124°W-100°W, 25°N-48°N] of the domain.

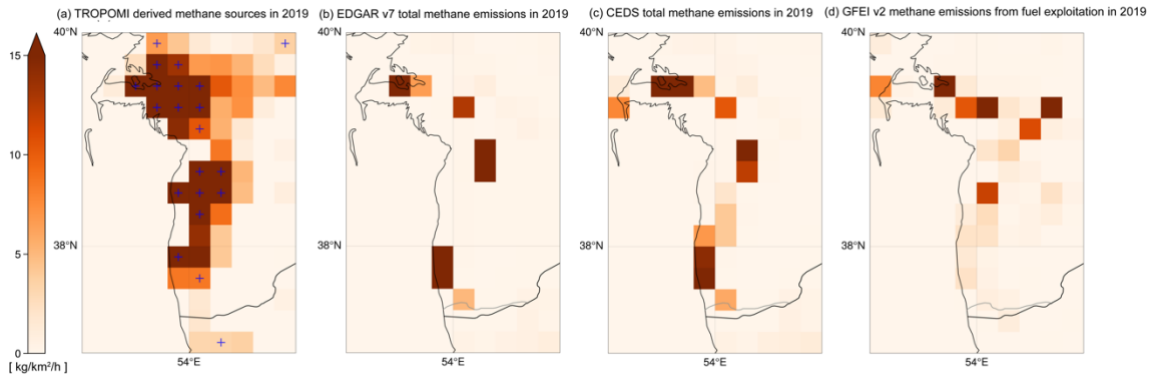

Figure S3. (a) The spatial distributions of annul methane emissions derived from TROPOMI XCH_4 over west of Turkmenistan in 2019. The sources passing the temporal filter are marked with blue "+". (b) EDGAR v7.0 averaged annual methane total emission in 2019. (c) CEDS v_2021_04_21 averaged annual total methane emissions in 2019. (d) GEFI v2 averaged annual methane emissions from the fuel exploitation in 2019.

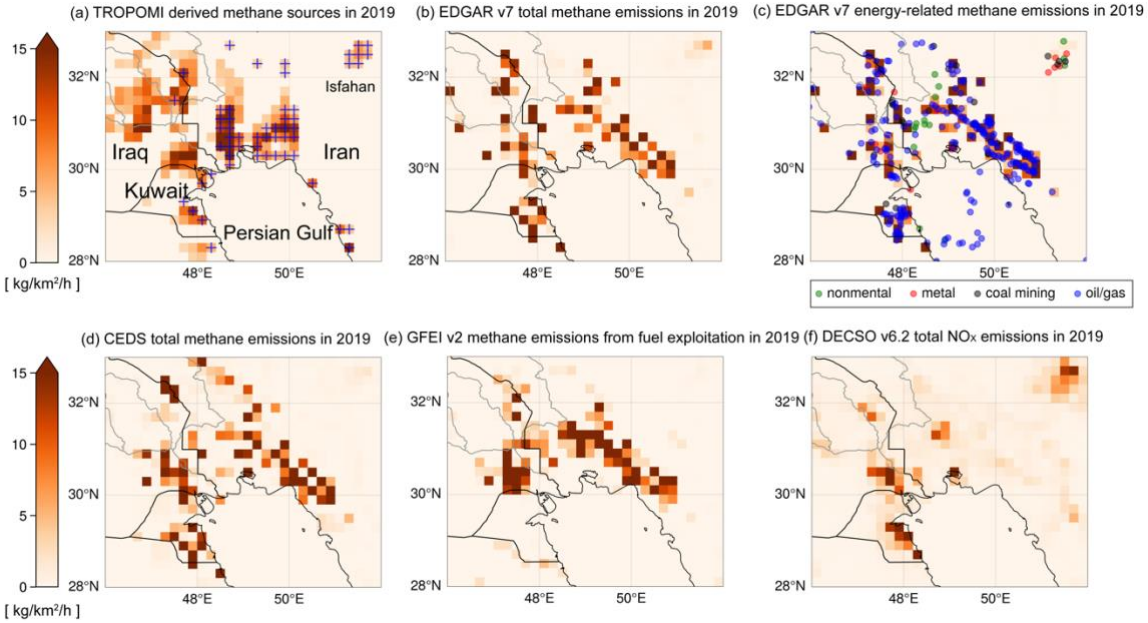

Figure S4. (a) The spatial distributions of annul methane emissions derived from TROPOMI XCH_4 over the coastal area of Iran, Iraq and Kuwait in 2019. The sources passing the temporal filter are marked with blue "+". (b) EDGAR v7.0 averaged annual methane total emission in 2019. (c)Energy-related methane emissions from EDGAR v7.0 overlapped with the industrial heat sources identified by VIIRS instrument. (d) CEDS v_2021_04_21 averaged annual total methane emissions in 2019. (e) GEFI v2 averaged annual methane emissions from the fuel exploitation in 2019. (f) Averaged annual DECSO v6.2 NO_X total emission in 2019.

Table S1. The annual emissions of EDGAR and TROPOMI

West of Turkmenistan [37.0°N, 53.0°E, 40°N, 55°E]				
kt/yr	2018	2019	2020	2021
EDGAR total	592	601	746	525
EDGAR energy	591	600	744	524
TROPOMI all sources	2826	2429	2426	2692
TROPOMI constant sources	1633	1544	1484	1413
Tehran [35.2°N, 50.6°E, 36°N, 52°E]				
kt/yr	2018	2019	2020	2021
EDGAR total	132	131	133	140
EDGAR energy	25	21	21	25
TROPOMI all sources	219	273	202	187
TROPOMI constant sources	147	207	178	153
Isfahan [32.4°N, 51.2°E, 32.8°N, 52.0°E]				
kt/yr	2018	2019	2020	2021
EDGAR total	32	32	32	35
EDGAR energy	10	9	9	12
TROPOMI all sources	129	113	112	126
TROPOMI constant sources	113	103	108	115
Iraq & Iran coastal area [29.6°N, 47.0°E, 32.6°N, 51°E]				
kt/yr	2018	2019	2020	2021
EDGAR total	4796	4327	4168	5102
EDGAR energy	4725	4255	4094	5026
TROPOMI all sources	3570	3484	3220	3781
TROPOMI constant sources	1037	1156	927	1280
Riyadh [24.4°N, 46.4°E, 25°N, 47°E]				
kt/yr	2018	2019	2020	2021
EDGAR total	264	267	276	280
EDGAR energy	66	64	69	67
TROPOMI all sources	171	184	177	188
TROPOMI constant sources	100	88	85	88

Table S2. The annual emissions derived with non-divergent and uncorrected wind

West of Turkmenistan [37.0°N, 53.0°E, 40°N, 55°E]				
kt/yr	2018	2019	2020	2021
EDGAR total	592	601	746	525
All sources (non-divergent *w*)	2826	2429	2426	2692
All sources (uncorrected *w*)	691	676	663	540
Tehran [35.2°N, 50.6°E, 36°N, 52°E]				
kt/yr	2018	2019	2020	2021
EDGAR total	132	131	133	140
All sources (non-divergent *w*)	219	273	202	187
All sources (uncorrected *w*)	202	214	165	185
Isfahan [32.4°N, 51.2°E, 32.8°N, 52.0°E]				
kt/yr	2018	2019	2020	2021
EDGAR total	32.00	32	32	35
All sources (non-divergent *w*)	129	113	112	126
All sources (uncorrected *w*)	122	87	104	113
Iraq & Iran coastal area [29.6°N, 47.0°E, 32.6°N, 51°E]				
kt/yr	2018	2019	2020	2021
EDGAR total	4796	4327	4168	5102
All sources (non-divergent *w*)	3570	3484	3220	3781
All sources (uncorrected *w*)	3079	2886	2363	3213
Riyadh [24.4°N, 46.4°E, 25°N, 47°E]				
kt/yr	2018	2019	2020	2021
EDGAR total	264	267	276	280
All sources (non-divergent *w*)	171	184	177	188
All sources (uncorrected *w*)	153	175	152	133